

Earth and Space Science



RESEARCH ARTICLE

10.1029/2021EA001966

Key Points:

- Over 11 years of Diviner data are compiled into gridded temperatures of the Lacus Mortis region
- Variations in radiative, thermophysical, and compositional properties are mapped and contrasting properties of materials are identified
- Temperatures within the Astrobotic Mission One landing ellipse suggest the regolith properties are similar to the global average

Correspondence to:

J.-P. Williams,
jpierre@mars.ucla.edu

Citation:

Williams, J.-P., Greenhagen, B. T., Bennett, K. A., Paige, D. A., Kumari, N., Ahrens, C. J., et al. (2022). Temperatures of the Lacus Mortis region of the Moon. *Earth and Space Science*, 9, e2021EA001966. <https://doi.org/10.1029/2021EA001966>

Received 13 AUG 2021

Accepted 17 DEC 2021






Author Contributions:

Conceptualization: Jean-Pierre Williams, Benjamin T. Greenhagen, Kristen A. Bennett, David A. Paige
Data curation: Patrick S. Russell, Mark T. Sullivan
Formal analysis: Jean-Pierre Williams, Paul O. Hayne
Investigation: Jean-Pierre Williams, Benjamin T. Greenhagen
Methodology: Jean-Pierre Williams, Benjamin T. Greenhagen
Resources: Nandita Kumari, Tyler M. Powell, David T. Blewett
Software: Jean-Pierre Williams, Benjamin T. Greenhagen, David A. Paige
Supervision: Jean-Pierre Williams, David A. Paige
Validation: Jean-Pierre Williams
Writing – original draft: Jean-Pierre Williams, Caitlin J. Ahrens

© 2021 The Authors.

This is an open access article under the terms of the [Creative Commons Attribution-NonCommercial License](#), which permits use, distribution and reproduction in any medium, provided the original work is properly cited and is not used for commercial purposes.

Temperatures of the Lacus Mortis Region of the Moon

Jean-Pierre Williams¹ , Benjamin T. Greenhagen², Kristen A. Bennett³ , David A. Paige¹, Nandita Kumari⁴, Caitlin J. Ahrens⁵ , Lior Rubanenko⁶, Tyler M. Powell¹, Parvathy Prem² , David T. Blewett² , Patrick S. Russell¹, Paul O. Hayne^{7,8}, and Mark T. Sullivan¹

¹Earth, Planetary, and Space Sciences, University of California Los Angeles, Los Angeles, CA, USA, ²Johns Hopkins University Applied Physics Laboratory, Laurel, MD, USA, ³U.S. Geological Survey, Astrogeology Science Center, Flagstaff, AZ, USA, ⁴Department of Geosciences, Stony Brook University, Stony Brook, NY, USA, ⁵Solar System Exploration Division, NASA Goddard Space Flight Center, Greenbelt, MD, USA, ⁶Department of Geological Sciences, Stanford University, Stanford, CA, USA, ⁷Astrophysical and Planetary Sciences, University of Colorado Boulder, Boulder, CO, USA, ⁸Laboratory for Atmospheric and Space Physics, University of Colorado Boulder, Boulder, CO, USA

Abstract Over 11 years of data acquired by the Diviner Lunar Radiometer Experiment instrument aboard Lunar Reconnaissance Orbiter have been compiled into a comprehensive data set of surface temperatures in the Lacus Mortis region which includes the landing ellipse of the Astrobotic Mission One lander mission. These data provide diurnal brightness temperatures at 128 pixels per degree (ppd) spatial resolution and 0.1 hr of local time resolution. From this data set, we highlight several features that display variations in radiative and thermophysical properties in the Lacus Mortis region and characterize the temperatures of the Astrobotic Mission One landing ellipse. We identify distinctly contrasting properties of materials in the walls of Bürg crater, hummocks of materials on the southeast margin of the mare basalts, and materials exposed or excavated by impacts. Additionally, we describe an exceptionally rocky fault scarp that predates the formation of Bürg crater suggesting the observed boulders are replenished on a timescale <1 Ga. Within the Astrobotic landing ellipse, temperatures are observed to range from ~88 to ~359 K with sunrise and sunset local times constrained to 5.8–6.3 hr and 17.8 and 18.1 hr respectively.

1. Introduction

The Diviner Lunar Radiometer Experiment on board the Lunar Reconnaissance Orbiter (LRO; Chin et al., 2007; Paige, Foote, et al., 2010; Tooley et al., 2010; Vondrak et al., 2010) has been acquiring brightness temperature measurements of the Moon near-continuously since July of 2009. This voluminous data set has enabled a global-scale characterization of the lunar thermal environment (Paige, Siegler, et al., 2010; Williams et al., 2017, 2019). With over 11 years of accumulated temperature measurements from orbit, we have compiled a cumulative data set focused on the Lacus Mortis region of the Moon which includes the location of Astrobotic's Peregrine Mission One landing site (Astrobotic, 2018).

Science, technology, and exploration payloads are planned to be delivered to the lunar surface starting in 2022 with an anticipated cadence for future deliveries to the lunar surface of approximately twice per year. Through the Science Mission Directorate's Commercial Lunar Payload Services (CLPS) initiative, NASA will procure commercial lunar delivery services and solicit lunar surface payloads to enhance our knowledge of the Moon and its potential resources (Bussey et al., 2019; Chavers et al., 2019). Before the utilization of lunar resources, the demonstration of lunar resource availability, extraction, refinement, and utilization properties must first be established (Thornton et al., 2015). Bringing these lunar resources to the forefront of lunar exploration requires a suite of missions, and an eventual infrastructure on the lunar surface. In November 2018, NASA selected nine providers through the CLPS program (Voosen, 2018) with additional payloads and experiments selected in 2019 (NASA, 2019a, 2019b). The first of these missions will be the Astrobotic Mission One which will be the first landed lunar mission by the United States since the Apollo program and the first commercial lunar lander to touch down on the Moon. Astrobotic provides lunar payload delivery service for the purpose of resource development-focused payloads integrated onto a single lunar lander (Thornton et al., 2015). Once on the surface, the payloads are deployed and activated, operate as a local utility, and provide power and communications as needed to the payloads. The target landing site for Mission One is Lacus Mortis (43.9142°N and 25.1476°E), a basaltic plain on the lunar nearside.

Writing – review & editing: Kristen A. Bennett, David A. Paige, Lior Rubanenko, Parvathy Prem, Paul O. Hayne

1.1. Lacus Mortis

Lacus Mortis is a ~160 km wide basin filled with mare basalt centered on 45.13°N and 27.32°E (Figure 1). The edges of the basin are characterized by relatively straight segments along the western half resulting in a hexagonal-like appearance. The mare deposits extend across the eastern edge and merge with Mare Frigoris to the north. The southern margin contains two heavily eroded craters, Plana and Mason, that also contain mare deposits within their interiors. The mare basalts of Lacus Mortis and neighboring Mare Frigoris are classified as Upper Imbrian (Scott, 1972; Wilhelms, 1987); have low TiO₂ and FeO and high MgO and Al₂O₃ abundances compared to other mare regions of the Moon (Kramer et al., 2015).

A considerable portion of the mare is disrupted by the 40 km diameter complex impact crater Bürg and its surrounding ejecta. Bürg is a Copernican-aged crater with a well-developed pattern of rays with several extending across Mare Serenitatis (Bart & Melosh, 2007). Averaged radial profiles of the Optical Maturity parameter of large rayed craters suggest Bürg is intermediate in age between Tycho (~109 Ma) and Copernicus (~810 Ma) craters (Grier et al., 2001), though crater size-frequency measurements by Terada et al. (2020) suggest a model age that exceeds 1 Ga. Earth-based radar shows that Bürg may be associated with a prominent low-return halo or radar-dark halo. However, the radar-dark area surrounding the crater corresponds with the boundaries of the mare basalt and a distinct dark halo boundary could not be resolved (Ghent et al., 2005).

The mare west of Bürg crater is tectonically complex with rilles, wrinkle ridges, elongated and linear depressions, and a pit. The most prominent of these features, the rille Rimae Bürg, extends beyond the southwest edge of the Lacus Mortis mare into the adjacent highlands materials and continues ~70 km across the mare interior before becoming muted by burial from the ejecta of Bürg crater, though a faint trace of the underlying feature can be identified on the ejecta for tens of kilometers. The rille comprises linear segments and a flat floor up to 2 km in width (Ostrach, 2011). Unlike sinuous rilles that are interpreted to be volcanic in origin (e.g., Carr, 1974; Greeley, 1971), Rimae Bürg is likely a structural graben of tectonic origin. The formation of large graben systems on the lunar nearside, like Rimae Bürg, are estimated to have ceased ~3.6 Ga (Lucchitta & Watkins, 1978), and Rimae Bürg can be inferred to predate the formation of Bürg crater due to the superposition of the crater's ejecta on the rille. A sizable pit has been identified within a kilometer of the graben at 44.962° and 25.610°E (Hong et al., 2015; Wagner & Robinson, 2012, 2014). The pit is elliptical in shape (~280 × 210 m) with a depth ~80 m, making it the largest pit identified on the Moon. Apparent collapse of the pit wall has formed a downward sloping ramp of material into the interior obscuring the eastern wall and any overhanging that may be present.

1.2. The Diviner Instrument

Diviner acquires radiometric measurements of the lunar surface in nine spectral bands over a wavelength range of 0.3–400 µm (Paige, Foote, et al., 2010). Each channel consists of 21-element linear arrays of thermopile detectors that are nominally nadir-pointing in a push broom configuration, though Diviner has independent elevation and azimuth actuators allowing for targeted observations. Channels 1 and 2 measure reflected solar radiation from 0.35 to 2.8 µm with differing sensitivities. Channels 3–5 have relatively narrow passbands around 8 µm utilized to identify the spectral location of the Christiansen feature, an emissivity maximum, that is diagnostic of bulk composition (Allen et al., 2012; Donaldson Hanna et al., 2012; Glotch et al., 2010, 2011; Greenhagen et al., 2010). Channels 6–9 measure thermally emitted radiation across four passbands covering 12.5–400 µm. Collectively, channels 3–9 allow for the characterization of the lunar thermal environment over a wide range of temperatures (~20–400 K) (Hayne et al., 2010; Paige, Siegler, et al., 2010; Williams et al., 2017).

2. Diviner Data Processing and Generation of the Lacus Mortis Data Set

Diviner Reduced Data Records (RDR) from infrared spectral channels 3–9 were used to generate a 128 pixels per degree (ppd) gridded data set for the Lacus Mortis region (41.5°–48.5°N and 22.5°–31.5°E). Each RDR record represents an individual detector observation and provides a calibrated radiance measurement obtained over a 0.128 s integration time with the most up-to-date calibration applied to the RDR data. The record contains an Activity Flag (“af”) field, which we used to constrain the data. The activity flag has a three-digit integer representing a combination of the orientation, observation type, and instrument mode (Sullivan et al., 2020). Values were constrained to 110–192 while emission angles were limited to <20° to minimize phase angle dependent radiative behavior of the lunar surface (Bandfield et al., 2011; Warren et al., 2019). While af = 110 represents

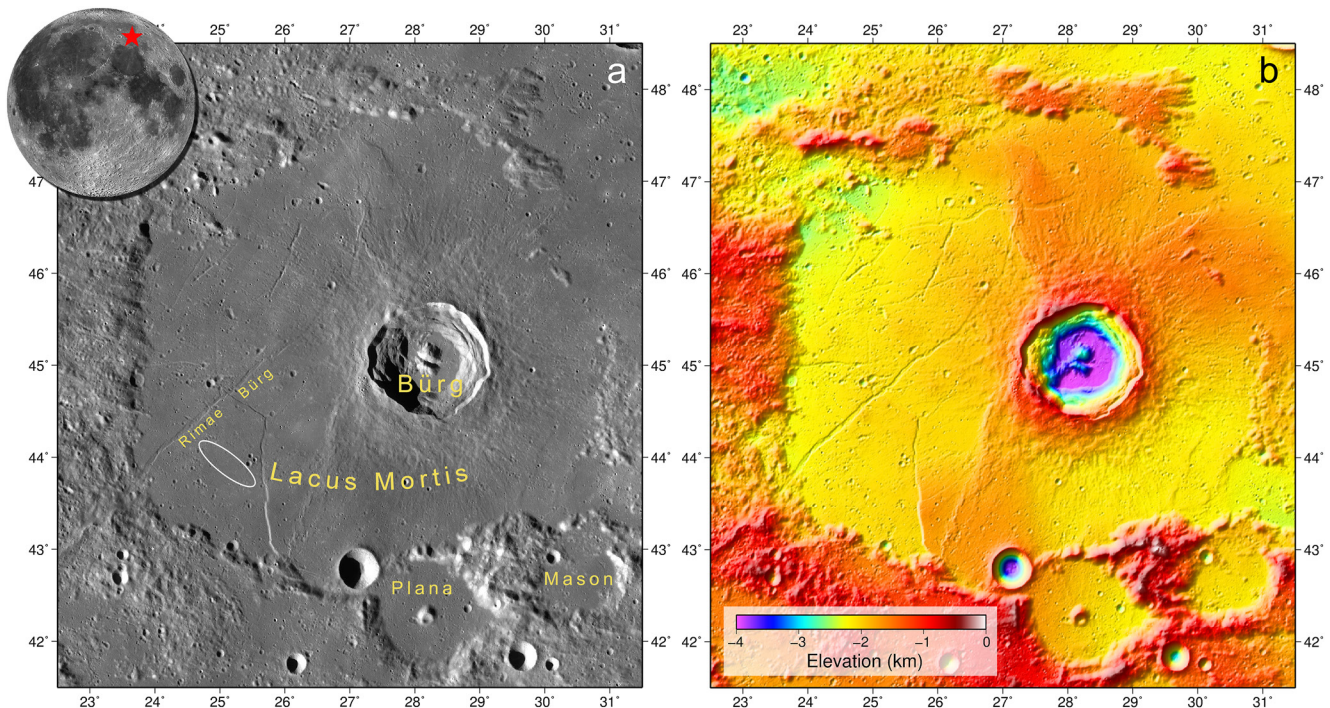


Figure 1. (a) A portion of the Lunar Reconnaissance Orbiter Camera (Robinson et al., 2010) Wide Angle Camera morphologic global mosaic with incidence angles between 55° and 75° (Speyerer et al., 2011; Wagner et al., 2015) showing the Lacus Mortis region in cylindrical equidistant projection with a standard parallel of 45°N. White ellipse is the location of Astrobotic's Mission One landing ellipse. Inset nearside globe with red star marks the location of Lacus Mortis. (b) Shaded relief of the Lacus Mortis region colored by elevation (SLDEM2015) (Barker et al., 2016).

nominal nadir-pointing operation, we extended the upper limit of the activity flag to include targeted observations with small emission angles including any observations potentially made as part of the Diviner “twilight campaign” to capture post-sunset observations (Russell et al., 2017, 2019). Several additional quality constraints were used (quality flag for calibration – 0; quality flag for miscellaneous – 0; noise quality flag – 0 to 1.5) (Sullivan et al., 2020).

The RDR records are represented by single locations on the surface; however, the total radiance that contributed to a measurement was derived from a finite area. To account for this during the binning process, the effective field-of-view (EFOV) for each record is estimated accounting for the elongation of the surface footprint in the in-track direction due to the thermal response time of the detectors and the spacecraft motion. This is done using the spacecraft altitude and velocity, and the individual channel instantaneous fields-of-view (see Williams et al., 2016 for details). A probability distribution is derived from the EFOV and used in a Monte Carlo simulation to ray-trace the EFOV onto a Lunar Orbiter Laser Altimeter (LOLA) digital elevation model (Smith et al., 2010) to account for the local terrain. We used 100 ray-traced points for each RDR record. Each point is assigned the same radiance value as the original observation and used as input to the binning routine. This aligns the different channels when binning because the positions of the fields-of-view for the individual channels are not identically aligned; therefore, each channel is not necessarily looking at the same location at a given instant (Paige, Foote, et al., 2010). Additionally, this ensures all bins within the EFOV are populated and, where adjacent detectors have overlapping EFOVs, captures the weighted mean of the observations that fall within a bin. Details of this process are described in Williams et al. (2016) and Sefton-Nash et al. (2017).

The data were processed in 1° tiles of longitude and latitude resulting in 63 files of binned data covering the Lacus Mortis region. The data within each tile were binned at 128 ppd in longitude and latitude and 0.1 hr in local time. To accommodate the EFOV modeling, a 2 bin (0.015625°) buffer exterior to the perimeter of each tile was included in the processing and trimmed after binning. A bin count cutoff of 10 was used to eliminate sparsely populated bins at the edges of the ground tracks that extend from the edge detectors in the EFOV modeling. This ensures the widths of the ground tracks are preserved (see Figure 4 of Williams et al., 2016). Only bins with radiance values

from all seven channels present were retained. Binned radiances were then converted to brightness temperatures, and the bolometric temperature (the equivalent blackbody temperature of the wavelength-integrated radiance from all seven channels) was calculated as described in Paige, Siegler, et al. (2010).

3. Results

3.1. Temperatures in Lacus Mortis

The binned bolometric temperatures provide diurnal temperatures at 0.1 hr local time resolution for each 128 ppd bin. Diurnal temperatures are generally well represented throughout the region though there are systematic differences in coverage (Figure 2). Local time coverage varies ~ 25 – 45% across the area with variations largely apparent as latitudinal striping. This striping results from differences in orbit track densities which are oriented approximately north-south due to the near-polar orbit of the spacecraft. The histogram of local time coverage for the region shows that a broad sampling of local times has been acquired in the area. Local times with a high number of observations are interspersed with local times where observations are infrequent or absent with the high and low observational densities alternating with a periodicity of ~ 2 hr in local time. Similar systematic local time gaps in coverage were noted by Williams et al. (2019) in the polar regions due to phasing of the spacecraft orbit.

Minimum temperatures are typically ~ 85 – 89 K throughout the region and occur in the early morning prior to sunrise (Figure 3). Maximum temperatures occur near noon and are ~ 345 – 365 K, approximately 30–40 K cooler than at the equator and are generally consistent with the predicted equilibrium maximum temperatures, 346–360 K, for the latitude range of our data, 41.5° – 48.5° N, assuming a solar constant $1,361 \text{ W m}^{-2}$, emissivity of 0.95, and the latitude dependent albedo from Vasavada et al. (2012). North-south facing slopes cause additional variability in the observed maximum temperatures as well as variations in the Sun-Moon distance which vary between 0.981 and 1.019 AU, predominantly due to the eccentricity of Earth's orbit. As the solar flux varies as the square of the Sun-Moon distance, this translates to $\Delta T_{\text{max}} \sim \pm 3.4$ K.

While daytime maximum temperatures are sensitive to the surface albedo, nighttime temperatures are sensitive to the thermophysical properties of the regolith within the diurnal thermal skin depth ~ 10 – 20 cm and will vary with the thermal inertia of the materials. Deviations in maximum and minimum temperatures are highlighted in Figure 3 by normalizing the temperatures by a latitude-dependent cosine function fit to the zonal mean minimum and maximum temperatures of the data. The vertical striping, most apparent in the normalized maximum temperatures, results from locations where orbit ground tracks did not cover the maximum temperatures around noon local time.

Gaps in local time coverage are particularly apparent in the hour before sunset and following sunrise when temperature changes are most rapid and slopes and shadows have the largest influence with changing illumination conditions. Temperature changes typically exceed 150 K in the hour after sunrise (6–7 hr) in Lacus Mortis and drop nearly the same amount the hour before sunset (17–18 hr). As a result, these periods of local time are the most challenging to resolve and have been the motivation for a campaign to target local times near sunset (~ 18 hr) (Russell et al., 2017, 2019).

3.2. Nighttime Anisothermality and Christiansen Feature

Differences in brightness temperatures between the Diviner infrared channels occur when there is a mixture of temperatures within a detector's field of view. Anisothermality in nighttime temperatures is indicative of surfaces of differing thermophysical properties radiating at different temperatures. Bandfield et al. (2011, 2017) utilized the anisothermality between channels 6, 7, and 8 to model rock and fine-grain regolith mixtures to estimate rock abundances and temperatures of regolith fines. Figure 4a shows the difference in brightness temperatures averaged over a 4-hr local time window centered on midnight between channels 6 and 8 ($T_6 - T_8$). Warmer temperatures in the instrument's field of view have an increased proportional influence on brightness temperatures in channels 6 relative to channel 8. Areas with higher $T_6 - T_8$ values represent locations where temperature contrasts are larger, for example, areas with mixtures of rocks and regolith fines with highly contrasting thermal inertias.

The radiances for channels 3–5 for local times between 10 a.m. and 2 p.m. including 358 orbits between 5 July 2009 and 10 June 2019 were used to generate a 128 ppd map of the Christiansen Feature (CF) (Figure 4b). The CF value represents the wavelength position of an emissivity maximum near $8 \mu\text{m}$ that is diagnostic of bulk

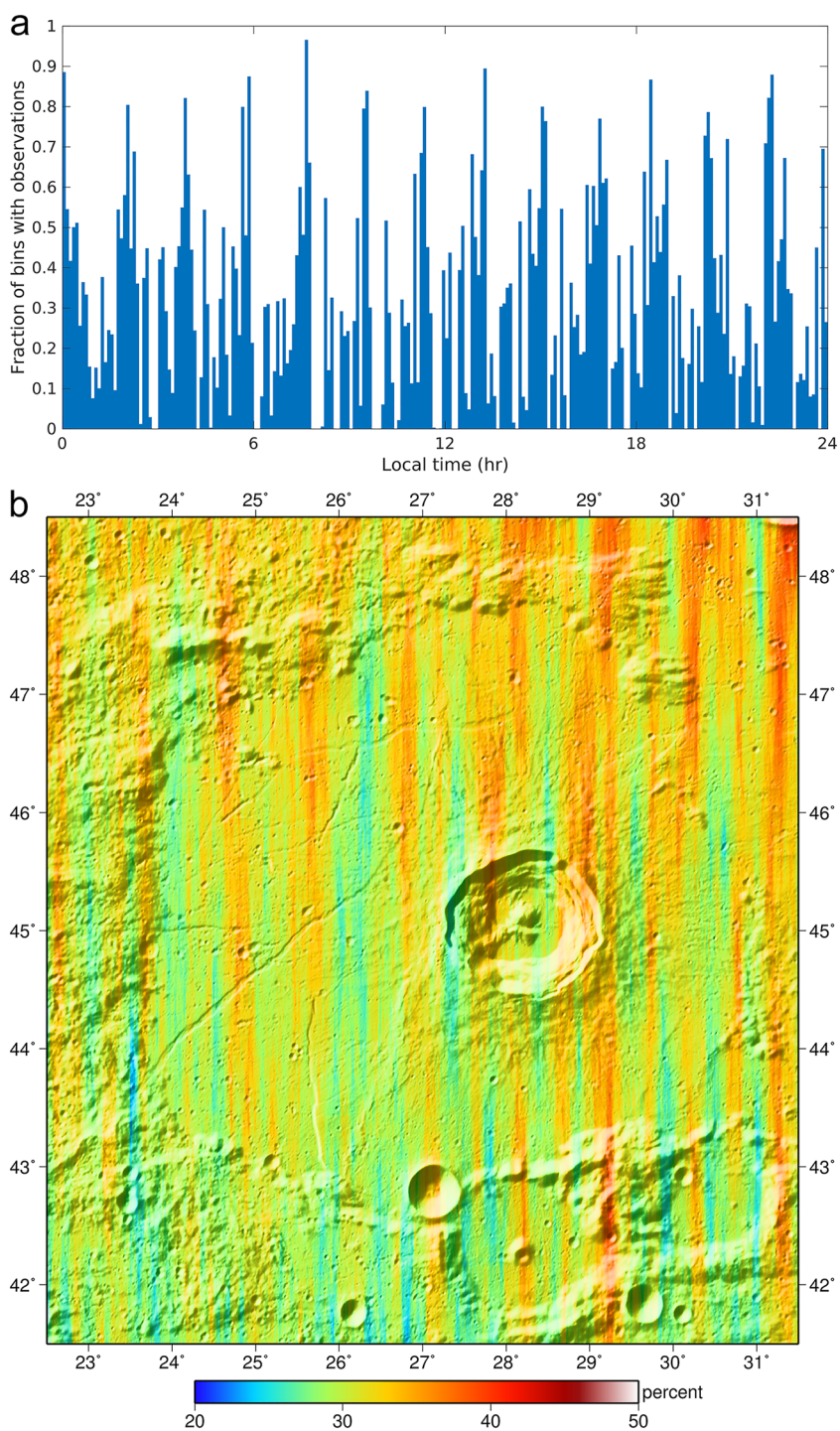


Figure 2. (a) A histogram of the 240 local time bins for the Lacus Mortis regions. (b) A map of the local time percent coverage (percentage of local time bins with data) of the region.

silicate mineralogy. The emission peak is shifted to shorter wavelengths for feldspathic lithologies, and conversely, shifted to longer wavelength for mafic lithologies. The CF value was calculated from a quadratic fit to the three Diviner channels for each bin (Greenhagen et al., 2010). Corrections to the CF were applied as described in Greenhagen et al. (2011) and Lucey et al. (2021) to account for photometric effects which can influence the

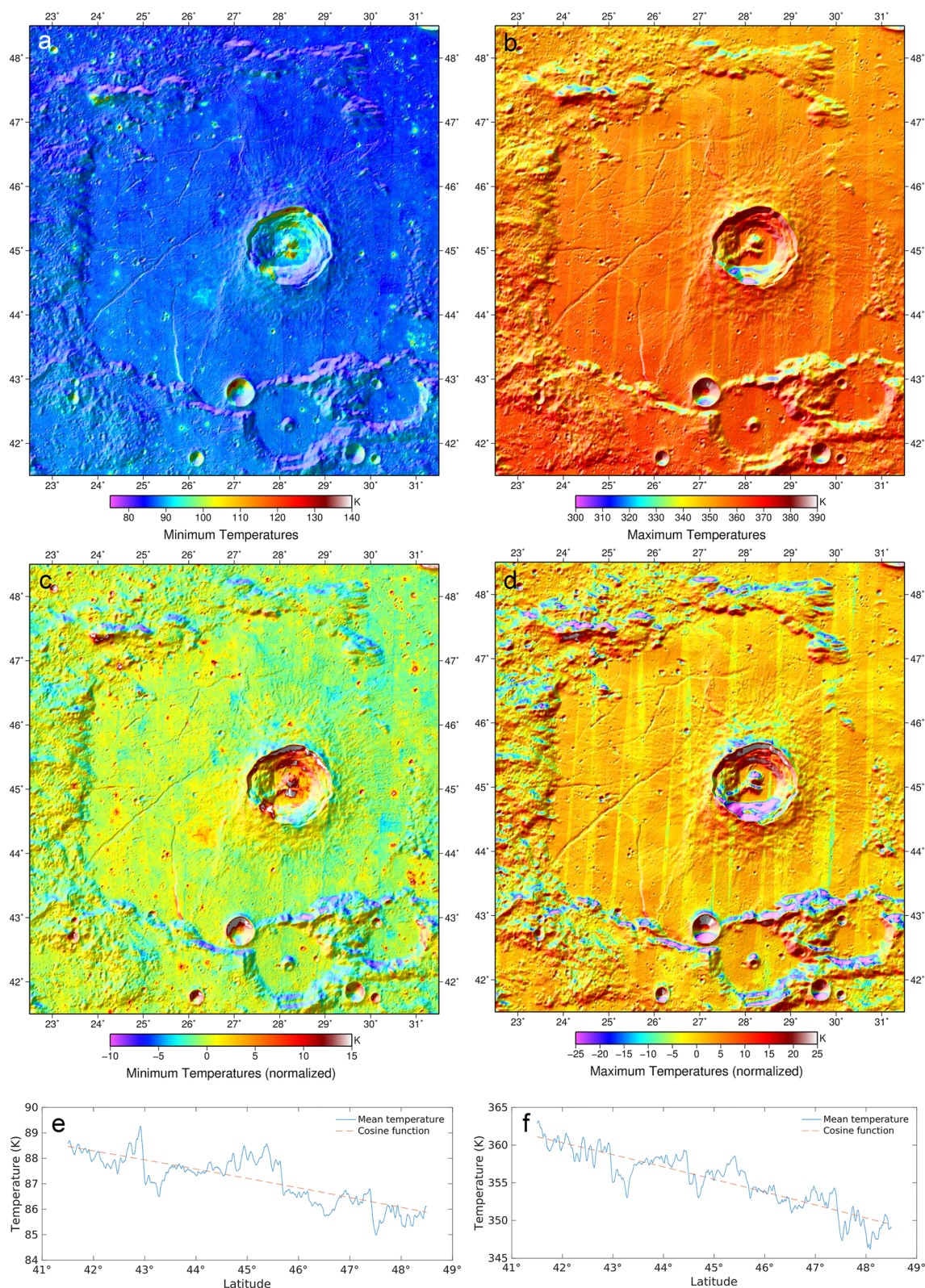


Figure 3. (a) Minimum and (b) maximum temperatures in Lacus Mortis. (c) Minimum and (d) maximum temperatures normalized by a cosine function fit to the zonal mean (e) minimum and (f) maximum temperatures.

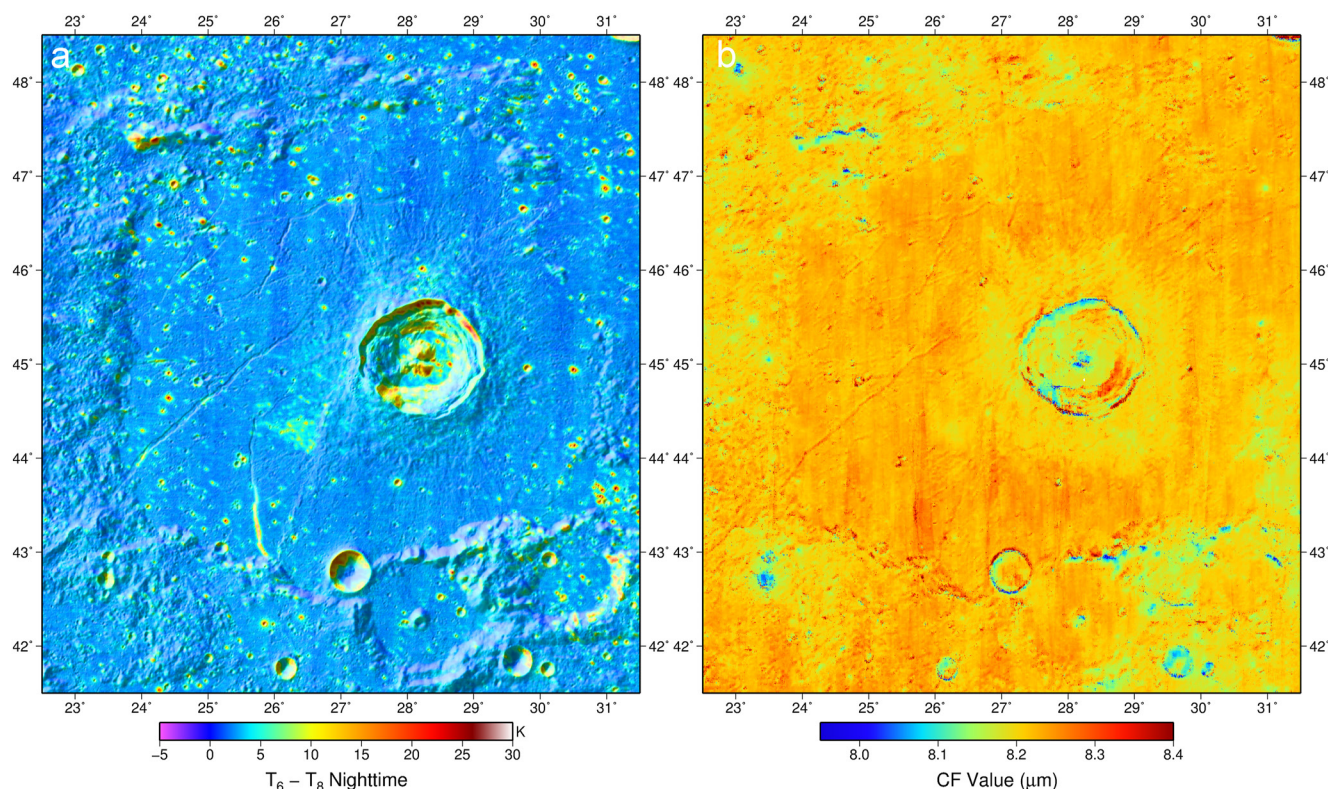


Figure 4. (a) Difference in nighttime temperatures between channels 6 and 8 ($T_6 - T_8$) highlighting variations in anisothermality in Lacus Mortis. (b) Christiansen Feature value normalized to equatorial noon derived from Diviner channels 3 to 5.

CF position. These data are analogous to the updated global 32 ppd normalized to equatorial noon archived data product (Greenhagen et al., 2021).

4. Discussion

4.1. Terrain Characterization

Surface materials can be broadly characterized by the normalized minimum and maximum temperatures which can vary with thermophysical properties and albedo where higher thermal inertia terrains sustain higher minimum temperatures during the night and darker surfaces attain higher peak temperatures during the day. To highlight these characteristics, we use the LROC WAC empirically normalized 643 nm single band mosaic, which has been photometrically normalized to a standard geometry (Boyd et al., 2012), and the normalized minimum and maximum temperatures to generate an RGB composite color map of the Lacus Mortis area (Figure 5). The individual maps were contrast enhanced using contrast-limited adaptive histogram equalization to improve the color balance (Pizer et al., 1987).

A general interpretation of the colors in Figure 5b is summarized in Figure 6. North-south slopes generally influence the overall trend in colors as equator-facing slopes will shift T_{\max} and T_{\min} to higher values resulting in a shift toward blue-cyan colors, that is, toward the upper-right quadrant of the color wheel in Figure 6. Conversely, slopes toward the pole will shift colors away from blue-cyan colors resulting in magenta, red, yellow, or green depending on albedo and thermal inertia. This can be seen around the walls of Bürg crater where the northern crater wall (equator-facing) is generally a cyan color while the southern wall (pole-facing) is predominantly red or yellow (Figure 5b).

Variations in colors in the southern wall reveal distinct heterogeneities in the materials of the wall (Figure 7). Much of the southern wall is red due to its poleward sloping surface reducing T_{\max} (blue) and T_{\min} (green). A relatively bright portion of the southwest wall is observed in the normalized LROC WAC mosaic. This area is

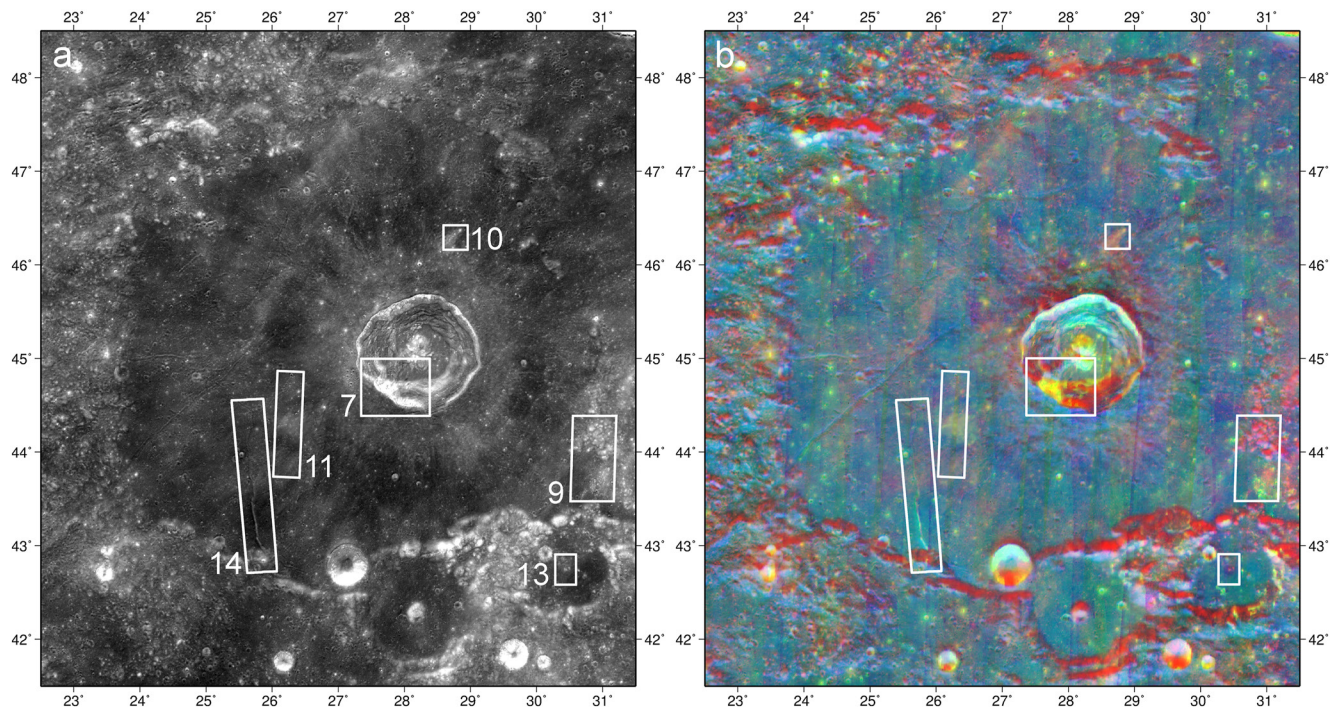


Figure 5. (a) Lunar Reconnaissance Orbiter Camera Wide Angle Camera (WAC) empirically normalized 643 nm single band mosaic of Lacus Mortis (Boyd et al., 2012). (b) RGB color composite map of Lacus Mortis with the normalized WAC mosaic in panel (a) used for the red channel, and the normalized minimum and maximum temperatures for the green and blue channels, respectively. The white boxes are the locations of figures indicated by the numbers.

warmer at night relative to the adjacent wall (Figure 7c) and displays greater nighttime anisothermality (Figure 7d) suggesting a component of high thermal inertia material, such as coherent rock, is concentrated in this portion of the wall. In the RGB composite map (Figure 7b), this portion of the wall shows up as yellow in the

brightest areas and green where surfaces are darker consistent with high thermal inertia materials with differing albedos (lower-right quadrant of the color wheel). The adjacent wall materials are red, with cooler T_{\min} and lower T_6-T_8 values consistent with more homogenized, lower thermal inertia materials. This portion of the wall also corresponds to a shift in CF values to shorter wavelengths (Figure 4) suggesting the composition in this portion of the wall is more feldspathic or felsic than adjacent portions of the wall. LROC Narrow Angle Camera (NAC) images (Figure 8) show that this portion of the wall is characterized by lighter toned material overlain by darker granular-to-blocky material that corresponds to the yellow and green colors in the RGB composite (Figure 7b) respectively.

A variety of terrain properties are observed on southeast margin of Lacus Mortis (Figure 9). Hummocky terrain along the margin of the mare appear as red/magenta in the RGB map suggesting they are bright with low thermal inertia. These colors persist on slopes both poleward and equatorward and cannot be attributed to slope effects. The adjacent mare (located to the southwest of the hummocky terrain) is blue/cyan due to its relatively low albedo except where a high density of craters are clustered. Colors in the crater clusters are shifted to orange/yellow/green representing a shift to higher thermal inertia materials with yellow representing bright material and green darker material. This can be seen in the crater in Figure 9d where bright, high-thermal inertia material has been exhumed and exposed in the crater walls on the western

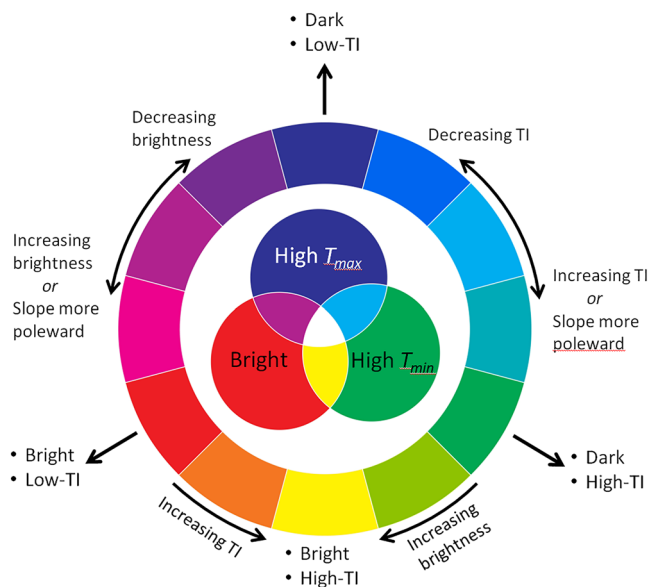


Figure 6. A color wheel presenting the general interpretation of the color trends in the RGB composite map of Lacus Mortis in Figure 5b where TI is thermal inertia. The red channel represents surface brightness, green represents T_{\min} , and blue represents T_{\max} .

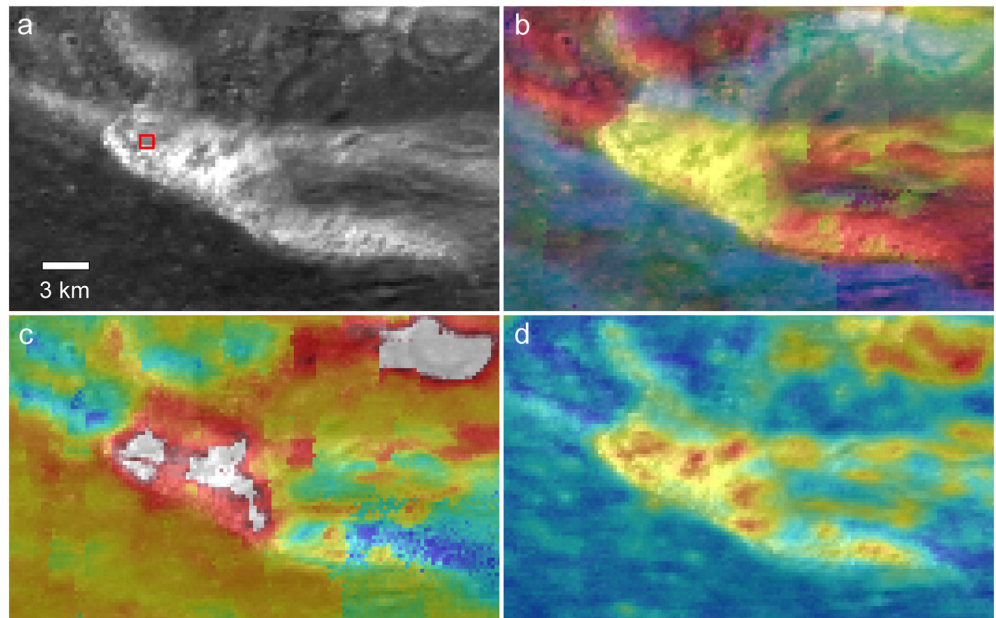


Figure 7. A portion of the southern rim of Bürg crater highlighting materials in the crater wall with contrasting properties: (a) Lunar Reconnaissance Orbiter Camera Wide Angle Camera empirically normalized 643 nm single band, (b) the RGB color composite map, (c) normalized minimum bolometric temperatures (T_{\min}), and (d) nighttime anisothermality ($T_6 - T_8$). See Figure 5 for location and Figures 3 and 4 for color scales. Red box in panel (a) is approximate location of Figure 8.

side but has been largely obscured on the eastern side by darker, high-thermal inertia material that has flowed down into the crater interior.

Craters that exhume blocky, immature materials from depth show up as shades of orange/yellow/green throughout the region as seen in the crater clusters in Figure 9. Other examples of crater clusters, possibly representing fields of secondary craters, are shown in Figures 10 and 11. The lunar near-surface regolith has been found to be highly insulating with low thermal conductivities and densities (e.g., Hayne et al., 2017; Vasavada et al., 2012). However, impacts can penetrate through the predominantly fine-grain upper surface materials to excavate more coherent rocky materials at depth (Elder et al., 2019; Hörz et al., 1991) which changes the thermophysical properties observed by Diviner as seen in the crater clusters (Figures 10 and 11). The influence of cratering on the thermophysical properties of the lunar surface are further demonstrated in Figure 12. Here, we plot the $T_6 - T_8$

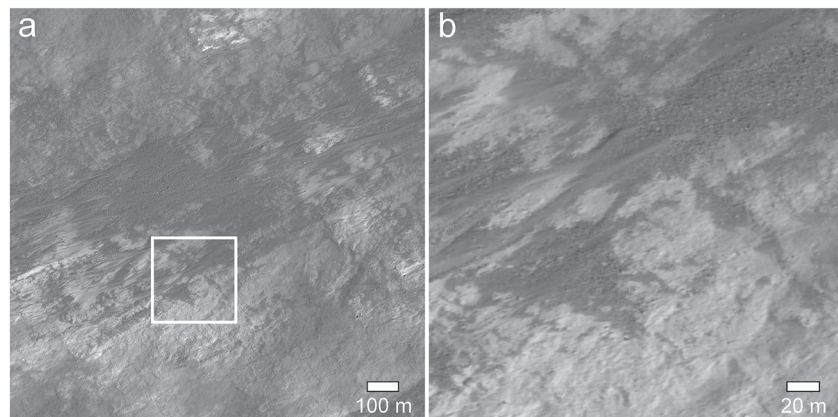


Figure 8. (a) A portion of Lunar Reconnaissance Orbiter Camera Narrow Angle Camera image M113778346R highlighting a portion of the Bürg crater wall with distinct thermophysical and compositional properties characterized by blocky and granular material interspersed on a brighter underlying material. The white box is the location of panel (b) showing the darker, overlying material comprised of granular material and blocks of varying sizes.

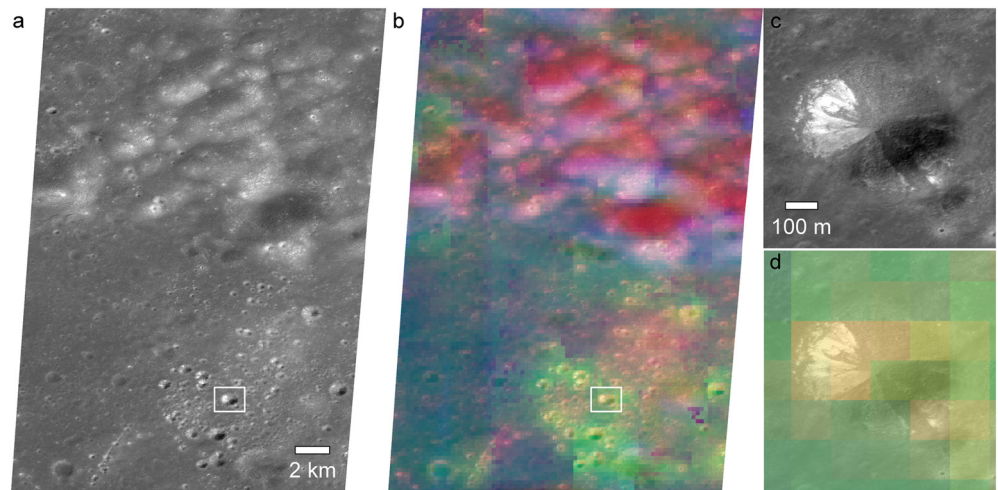


Figure 9. (a) A portion of Lunar Reconnaissance Orbiter Camera Narrow Angle Camera image pair m1182282635 showing hummocky terrain along the southeast margin of the mare basalt in Lacus Mortis. (b) The image colorized with the RGB composite map showing the contrasting properties of the hummocky terrain and the mare, and the mare where it has been disrupted by clusters of craters. Panel (c) subframe of panel (a) highlighting one of the larger craters in the cluster and panel (d) a subframe of panel (b) showing the same crater. See Figure 5 for location. North is up in all images.

nighttime anisothermality versus the maximum temperatures for slopes $<2^\circ$ to eliminate the influence of topography. There is a distinct trend in the temperature amplitude ($T_{\max} - T_{\min}$) experienced by a surface. The anisothermality is a proxy for rockiness with higher values indicating a greater fraction of rocks (Figure 12b). These areas tend to correlate with brighter, more immature surfaces as rocks break down in the space environment and regolith matures and darkens (e.g., Fischer & Pieters, 1996; Hörz et al., 2000; Lucey et al., 2000). Fresh, rocky ejecta will plot toward the lower right on the figure (blue symbols) and overtime, will migrate toward the upper left (red symbols) as rocks are commuted into regolith (shift left) and surfaces are space weathered and darkened (shift up).

Cold spots associated with young, recently formed impact craters also appear distinctive in the RGB color map. Cold spots are observed as extensive annuli of anomalously cold nighttime temperatures around young craters (Bandfield et al., 2011, 2014). Cold spots are estimated to fade within ~ 1 Ma, possibly due to impact gardening, and thus represent fairly ephemeral features on the lunar surface (Williams et al., 2018). Figure 13 shows a 200-m crater at 42.745°N and 30.430°E on the mare deposits within the floor of Mason crater with a ~ 4 km wide cold spot. The cold spot has a $\sim 3\text{--}4$ K lower minimum temperature than the surrounding terrain, and the transition from the cyan color of the surrounding mare deposits to blue and magenta on the cold spot in the RGB map results from a decrease in thermal inertia in the cold spot.

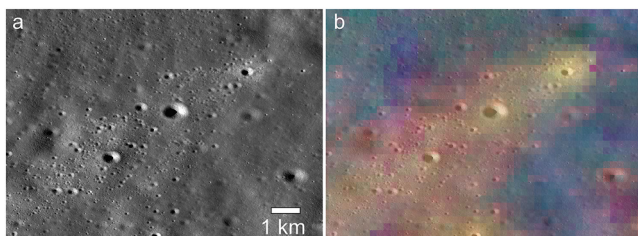


Figure 10. (a) A portion of Lunar Reconnaissance Orbiter Camera Narrow Angle Camera image pair m1338656930 showing a cluster of craters north of Bürg crater and (b) the image colorized with the RGB composite map. The yellow/orange coloration of the cluster results from brighter, higher thermal inertia materials within the cluster. See Figure 5 for location.

In addition to young impact craters, high densities of blocks are observed along fault scarps (Figure 14). A prominent ~ 60 km long north-south trending fault transects the southwest floor of Lacus Mortis intersecting Rimae Bürg to the north. The southern ~ 20 km of the fault has a west-facing scarp with a vertical offset of ~ 350 m. The fault scarp is characterized by high $T_6 - T_8$ values resulting from the numerous boulders observed on the scarp face (Figure 14e). The RGB color shift across the scarp, that is, blue to cyan/green, is consistent with a shift to higher thermal inertias. The fault changes dip and offset sense along strike to the north indicating a rotational component to the relative displacement with an axis of rotation perpendicular to the plane of failure (scissor failure). A perpendicular fault trace extending eastward from the scarp coincides with an offset in the strike of the fault scarp suggesting a possible right-lateral displacement (white arrow in Figure 14). Approximately 10 km north of this offset where the fault blocks are nearly the same elevation, both fault blocks are separated by a depression up

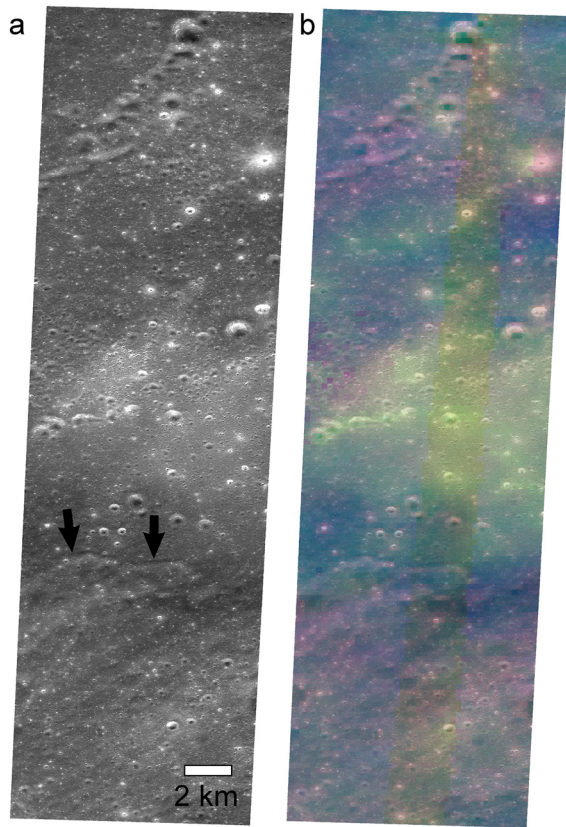


Figure 11. (a) Lunar Reconnaissance Orbiter Camera Narrow Angle Camera image m1118717657L centered on a clustering of craters southeast of Bürg crater and (b) the image colorized with the RGB composite map. The yellow/green coloration results from excavation of immature brighter, higher thermal inertia materials by the impacts. Other craters with more degraded appearances, including an alignment of pits or heavily degraded crater near the top of the figure, do not show the same distinctive color signature. Terrain with a hummocky texture in the lower third of the image has a distinct magenta coloration (black arrows) relative to the adjacent blue mare basalt. See Figure 5 for location.

to ~80 m depth suggesting extension occurred along this portion of the fault, possibly related to the perpendicular fault trace apparent in the east block to the south.

Terrain with a hummocky texture is observed across the fault scarp. The RGB map shows a shift away from blue-cyan colors (reddening) for the hummocky surface texture. The southern margin of this color shift is indicated with black arrows in Figure 14d. The topographic relief of the scarp becomes subdued and the anisothermality drops to background levels here. This hummocky material is also seen in Figure 11 and appears to be part of a larger region of material red-shifted in the RGB map (Figure 5) with a general radial orientation to Bürg crater and may represent material mobilized by the crater forming impact.

The scarp age therefore likely pre-dates the formation of Bürg crater making it pre-Copernican in age (i.e., >1 Ga). The survival times of meter-scale boulders against collisional destruction in the lunar environment is estimated to be much less than 1 Gyr with 99% of meter-scale ejecta boulders estimated to be destroyed after only ~200–300 Ma (Basilevsky et al., 2013, 2015) with the thermal signatures associated with rocky ejecta observed to generally fade to background levels of nominal regolith within ~1 Ga (Ghent et al., 2014). The sustained presence of a significant concentration of boulders along the scarp therefore suggests boulders are being replenished on timescales much shorter than this.

4.2. Landing Site Temperatures

The landing ellipse for Mission One is 24×6 km within a relatively flat southwest portion of Lacus Mortis centered on 43.9142°N and 25.1476°E (Figure 15) (Astrobotic, 2018). There is a modest decline in elevation of ~100 m from the southeast to the northwest portion of the ellipse (Figure 15b). The ellipse area is devoid of any large variations in thermophysical properties suggesting a relatively benign region for landing relative to the surrounding areas containing larger craters and scarps. The nighttime anisothermality within the ellipse is relatively low and uniform and colors in the RGB composite are similar to areas characterized by relatively undisturbed mare elsewhere in Lacus Mortis (Figures 15c and 15d). Therefore, the thermophysical properties of the materials within the ellipse are likely

representative of the broader mare at the mapped scale of 128 ppd. At smaller scales, craters could have excavated blocks at small enough sizes and/or low enough concentrations to not generate a significant anisothermal signal in the Diviner data. Craters on the margins of the ellipse are observed to have elevated anisothermality signatures suggesting they are associated with rocky materials. These craters likely would have ejected some blocks into the ellipse area.

The mean diurnal temperatures within the ellipse are plotted in Figure 16 with error bars showing the standard deviation of the temperatures for a given local time bin. Temperatures range from a minimum of ~88 K just prior to sunrise to a maximum of ~359 K near local noon. The mission is planned to land mid-morning, ~7.8–9.7 hr, local time (55–110 Earth hours after sunrise) (Astrobotic, 2018). Within this local time window, temperatures within the ellipse area will already generally exceed 300 K with many locations >330 K. At local time 5.8–5.9 hr, temperatures are 88.4 ± 0.5 K; at local time 6.2–6.3 hr, temperatures are 167.2 ± 4.0 K. The intervening time bins do not contain any observations. The sudden increase in temperature ($\Delta T = 78.8$ K) between these local times indicates they bracket the time of sunrise within the ellipse. Similarly, the maximum rate of temperature change in the afternoon hours occurs between 17.8 and 18.1 hr where temperatures decrease from 183.2 ± 11.4 to 120.4 ± 2.3 K due to sunset. After this time, the rate of cooling is much more limited and determined by the balance of heat stored in the near-surface regolith layers to the loss of radiation to space during the night. Therefore, temperatures after sunset will be sensitive to the thermophysical properties of the regolith (Hayne

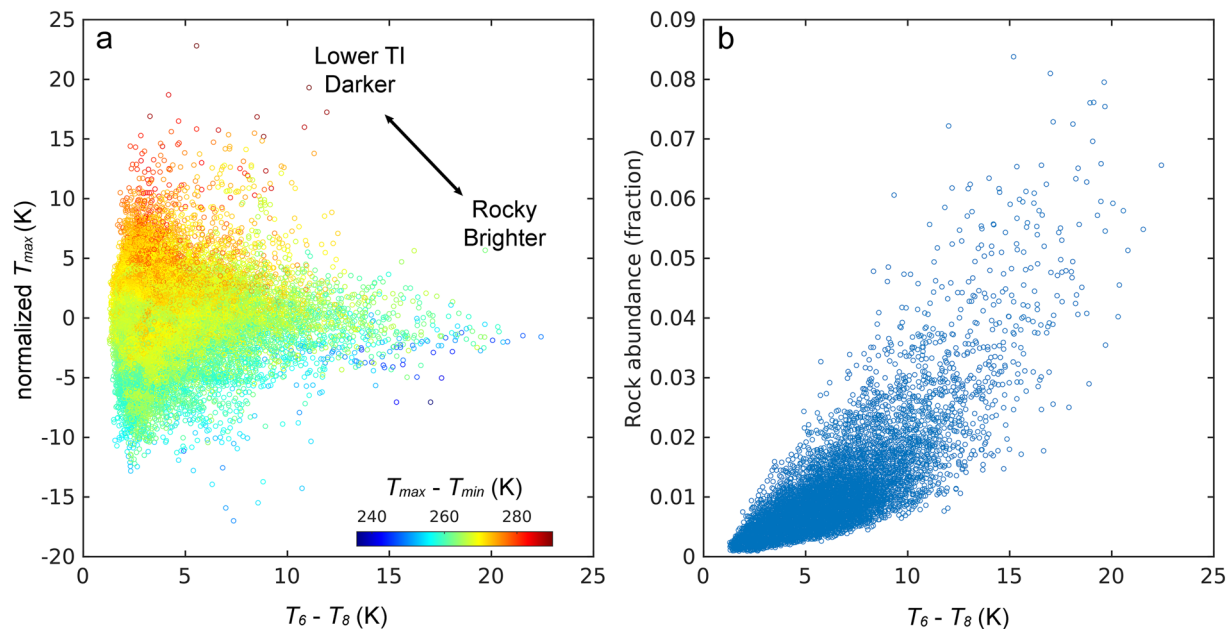


Figure 12. (a) A scatter-plot of nighttime anisothermality ($T_6 - T_8$) versus normalized maximum temperatures (T_{max}) for slopes $<2^\circ$ in Lacus Mortis with symbol colors representing the temperature amplitudes ($T_{max} - T_{min}$). (b) A scatter-plot of nighttime anisothermality ($T_6 - T_8$) versus modeled rock abundance from Bandfield et al. (2011, 2017).

et al., 2017; Williams et al., 2017). The regolith thermal model of Hayne et al. (2017) closely overlaps the landing ellipse temperatures where we have assumed nominal regolith values as described in Hayne et al. (2017) with the incidence angle dependent albedo from Vasavada et al. (2012) appropriate for mare surfaces. This suggests the regolith properties within the ellipse are generally similar to the global average (Figure 16). The model predicts minimum and maximum temperatures of 87 and 349 K respectively with the amplitude of the temperature variations damping out rapidly with depth (within ~ 20 cm). Global modeling by Hayne et al. (2017) find the upper regolith thermal inertia to be remarkably uniform at the global scale and we anticipate the upper regolith to be similar to the Apollo sites which yield similar density profiles as the nominal model used here.

Predicted morning and afternoon temperatures tend to be cooler than the observed bolometric temperatures. Anisothermality in the Diviner spectral channels have been shown to correlate with solar incidence (Bandfield

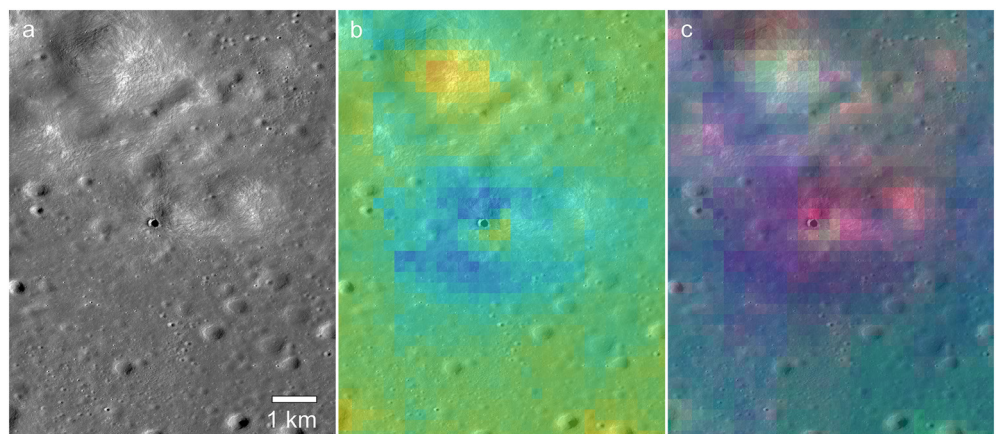


Figure 13. (a) A portion of Lunar Reconnaissance Orbiter Camera Narrow Angle Camera (NAC) image m1215240241R centered on a 200-m diameter crater associated with a cold spot on the floor of Mason crater. (b) The NAC image colorized with the normalized minimum temperatures (see Figure 3 for color scale), and (c) the RGB color map showing the cold spot. See Figure 5 for location.

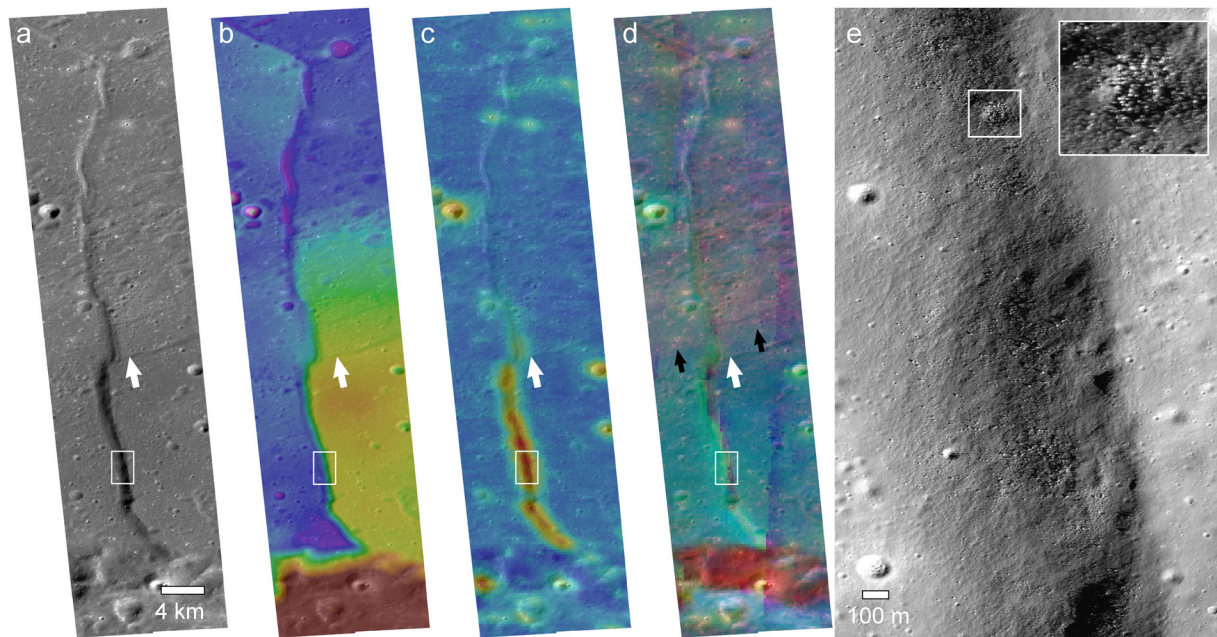


Figure 14. (a) Lunar Reconnaissance Orbiter Camera Narrow Angle Camera image pair m1258763011 showing a ~60 km north-south trending fault scarp in the southwest floor of Lacus Mortis. The images are colorized with (b) topography (SLDEM2015), (c) nighttime anisothermality ($T_6 - T_8$) (see colorbar in Figure 4), and (d) the RGB composite map (see Figures 5b and 6 for explanation of colors). The white box shows the location of panel (e) highlighting a portion of image m1258763011R along the fault scarp where numerous blocks are visible and anisothermality is elevated. ~350 m of vertical relief occurs along the scarp at this location. Inset highlights the high density of boulders on the scarp. The white arrows in panels (a–d) indicate the location of a perpendicular fault apparent in image and topography data that correspond with an offset in the strike of the scarp. Black arrows in panel (d) denote the approximate southern extent of “red-shifted” hummocky material that appears to overlay the fault. See Figure 5 for location. North is up in all figures.

et al., 2015; Williams et al., 2017) due to surface roughness. Variations in orientations of shaded and sunlit slopes with respect to the sun result in mixtures of temperatures within a detector's field of view which elevate the brightness temperatures of the shorter wavelength channels. This increase in blue spectral slope is seen across the lunar surface in both the highlands and mare and will result in warmer bolometric temperatures in the morning and afternoon. Such effects due to roughness have not been accounted for in the model.

The Near-Infrared Spectrometer System (NIRVSS; Roush et al., 2015) on the payload will provide the opportunity to explore the range of temperatures that occur within the ellipse at subpixel-scales and help constrain surface properties. The objective of the NIRVSS instrument is to observe surface mineralogy and volatiles and characterize surface morphology and thermophysical properties. The short-wave and long-wave spectrometers cover the 1,200–2,400 and 2,300–4,000 nm (with spectral resolutions of <20 and <50 nm), respectively (Roush et al., 2020).

5. Summary

We have compiled over 11 years of brightness temperature data acquired by the Diviner instrument aboard LRO into a comprehensive data set of surface temperatures in the Lacus Mortis region containing the Astrobotic Mission One landing site. These data provide diurnal brightness temperatures at 128 ppd spatial resolution and 0.1 hr of local time resolution for the Diviner instrument's seven infrared spectral channels and the corresponding bolometric temperatures. From these data, we generate several maps of the region: minimum and maximum bolometric temperatures normalized by a latitude dependent function fit to the zonal mean temperatures, the channels 6 and 8 nighttime anisothermality, and a color composite image using the WAC empirically normalized 643 nm single band mosaic and the normalized minimum and maximum bolometric temperatures. Collectively, these maps highlight variations in radiative and thermophysical properties of the region.

The thermal response of the materials within Lacus Mortis as seen in our data are generally consistent with the comminution and space weathering of materials over time that result in an evolutionary trend toward finer-grain,

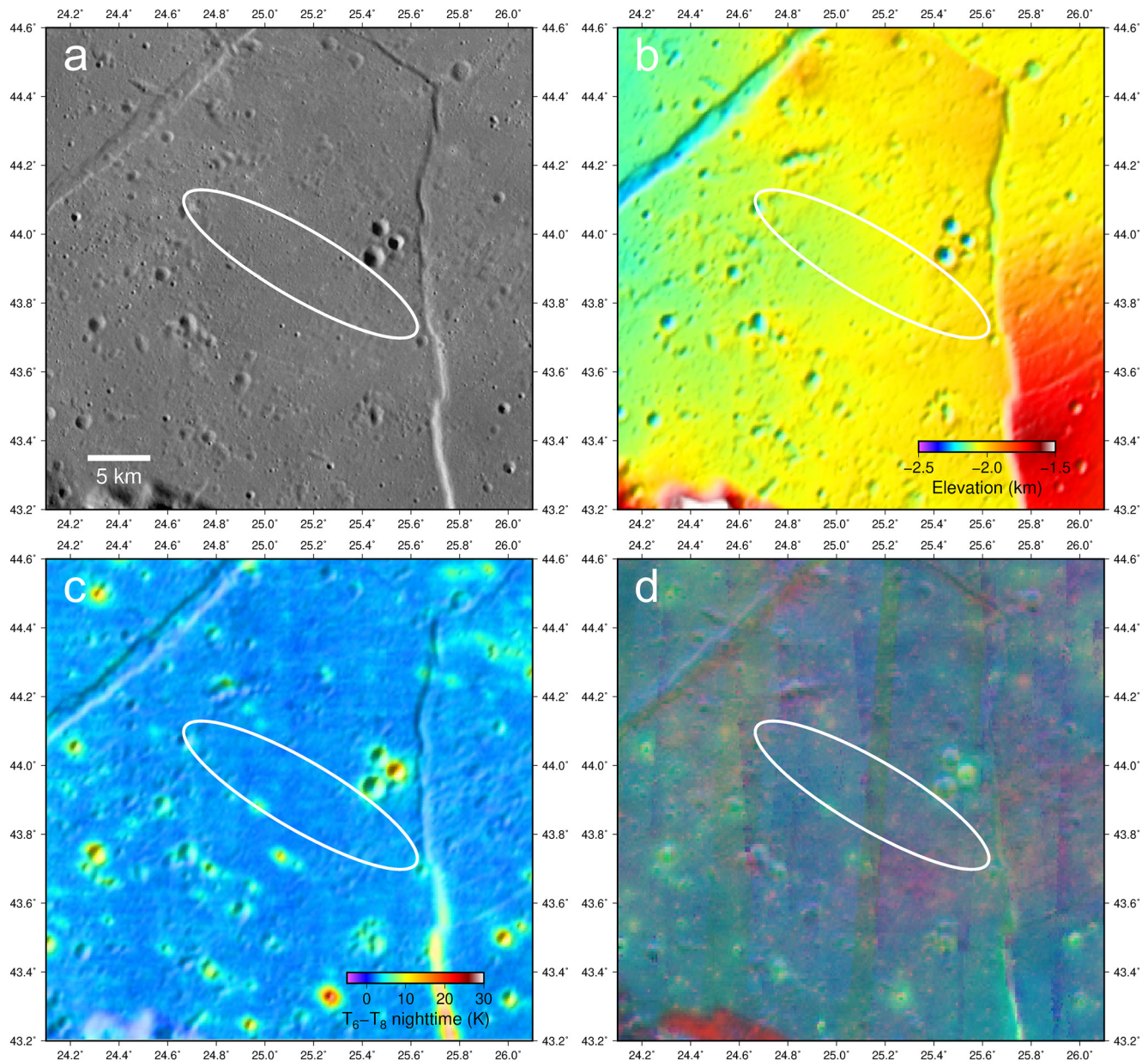


Figure 15. (a) Lunar Reconnaissance Orbiter Camera Wide Angle Camera mosaic, (b) shaded relief of the Lacus Mortis region colored by elevation (SLDEM2015), (c) $T_6 - T_8$ nighttime anisothermality, and (d) RGB composite map (see Figures 5b and 6 for explanation of colors) with the approximate Astrobotic Mission One landing ellipse (Astrobotic, 2018) in the southwest portion of Lacus Mortis.

darker materials. We identify a diversity of material properties along the south wall of Bürg crater. A portion of the wall that corresponds to a higher reflectance in WAC image data is found to have a higher thermal inertia with a greater abundance of thermally contrasting materials relative to other parts of the wall. On the eastern margin of Lacus Mortis, we find hummocks of material with distinctly contrasting properties with the adjacent mare basalt deposits and are both higher albedo and low thermal inertia than typically observed in the region. Impacts and impact clusters are readily identified in the data as they excavate both bright and dark high-thermal inertia materials from beneath the surface regolith layer. Cold spots are also identifiable as anomalously low thermal inertia patches of regolith surrounding craters with a relatively fresh morphology. We highlight a 200-m diameter crater with a ~4 km wide cold spot. The presence of a cold spot at a crater of this size constrains the formation of the crater to within the last ~200 kyr (Williams et al., 2018).

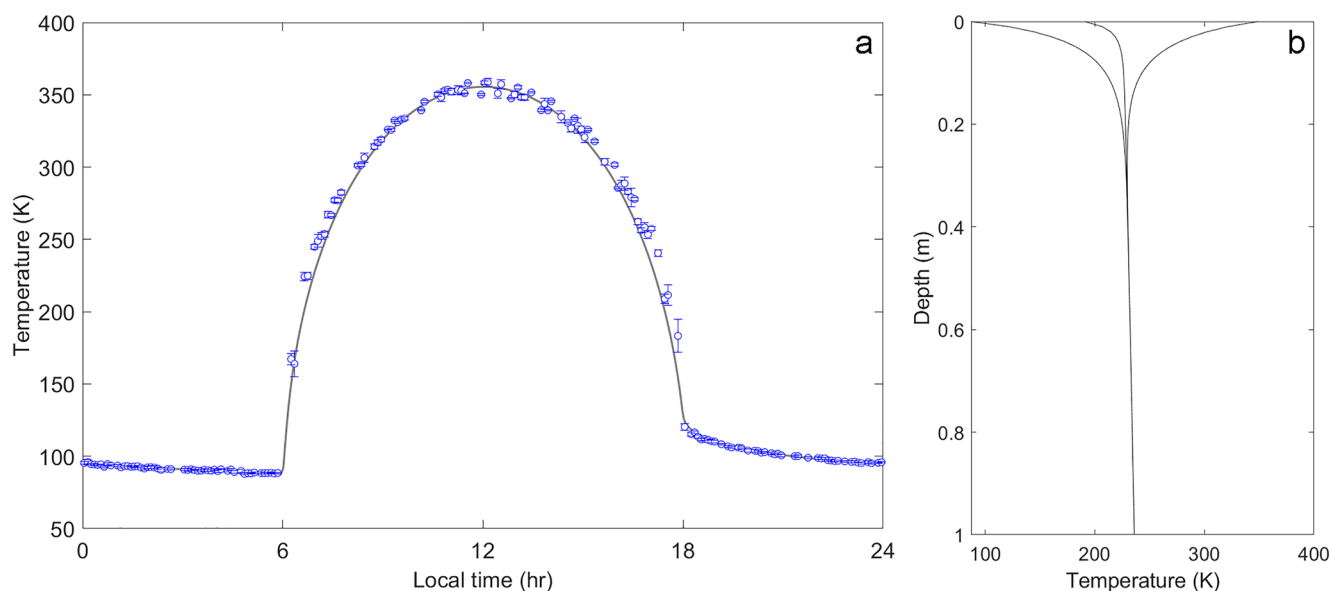


Figure 16. (a) Mean bolometric temperatures calculated from the landing ellipse in Figure 15. Error bars reflect the standard deviation for the local time bins. The gray curve is the nominal Hayne et al. (2017) regolith thermal model assuming the incidence angle dependent albedo of Vasavada et al. (2012). (b) Model minimum, mean, and maximum temperatures with depth.

A relatively high density of boulders is identified along a segment of ~60 km fault scarp in the southwest portion of Lacus Mortis. A ~20 km segment of the fault scarp is associated with significant nighttime anisothermality, which is confirmed to correlate with high densities of boulders visible in LROC NAC images. A portion of the scarp is overprinted by a thermally distinct hummocky deposit that appears to be the result of material mobilized by the Bürg crater-forming impact event.

Temperatures within the estimated Astrobot Mission One landing ellipse range from a minimum of ~88 K to a maximum of ~359 K. Surface temperatures in the estimated local time window predicted for landing are observed to be ~300–335 K. Based on the rate of change in the diurnal temperatures, we estimated sunrise and sunset times to occur between 5.8–6.3 hr and 17.8 and 18.1 hr, respectively.

Data Availability Statement

The Reduced Data Records data used in this study (Paige, 2010) are publicly available via the Geosciences Node of the Planetary Data System (<http://pds-geosciences.wustl.edu/missions/lro/diviner.htm>), and the gridded data generated for this study and supporting maps generated from the gridded data are available from the UCLA Diviner supporting online data repository (www.diviner.ucla.edu/published-datasets).

Acknowledgments

The authors thank the LRO Diviner, LROC, and LOLA operations team for their effort in returning the data presented here and two anonymous reviewers whose constructive comments and feedback improved the manuscript. This work was supported by the Lunar Reconnaissance Orbiter Project and the Diviner science investigation, under contract with the NASA.

References

- Allen, C. C., Greenhagen, B. T., Hanna Donaldson, K. L., & Paige, D. A. (2012). Analysis of lunar pyroclastic deposit FeO abundances by LRO Diviner. *Journal of Geophysical Research*, 117, E00H28. <https://doi.org/10.1029/2011JE003982>
- Astrobotic. (2018). Peregrine Lunar Lander payload user's guide, Version 3.0. <https://www.astrobotic.com/>
- Bandfield, J. L., Cahill, J. T., Carter, L. M., Neish, C. D., Patterson, G. W., Williams, J. P., & Paige, D. A. (2017). Distal ejecta from lunar impacts: Extensive regions of rocky deposits. *Icarus*, 283, 282–299. <https://doi.org/10.1016/j.icarus.2016.05.013>
- Bandfield, J. L., Ghent, R. R., Vasavada, A. R., Paige, D. A., Lawrence, S. J., & Robinson, M. S. (2011). Lunar surface rock abundance and regolith fines temperatures derived from LRO Diviner radiometer data. *Journal of Geophysical Research*, 116, E00H02. <https://doi.org/10.1029/2011JE003866>
- Bandfield, J. L., Hayne, P. O., Williams, J.-P., Greenhagen, B. T., & Paige, D. A. (2015). Lunar surface roughness derived from LRO Diviner Radiometer observations. *Icarus*, 248, 357–372. <https://doi.org/10.1016/j.icarus.2014.11.009>
- Bandfield, J. L., Song, E., Hayne, P. O., Brand, B. D., Ghent, R. R., Vasavada, A. R., & Paige, D. A. (2014). Lunar cold spots: Granular flow features and extensive insulating materials surrounding young craters. *Icarus*, 231, 221–231. <https://doi.org/10.1016/j.icarus.2013.12.017>
- Barker, M. K., Mazarico, E., Neumann, G. A., Zuber, M. T., Haruyama, J., & Smith, D. E. (2016). A new lunar digital elevation model from the Lunar Orbiter Laser Altimeter and SELENE Terrain Camera. *Icarus*, 273, 346–355. <https://doi.org/10.1016/j.icarus.2015.07.039>
- Bart, G. D., & Melosh, H. J. (2007). Using lunar boulders to distinguish primary from distant secondary impact craters. *Geophysical Research Letters*, 34, L07203. <https://doi.org/10.1029/2007gl029306>

- Basilevsky, A. T., Head, J. W., & Hörz, F. (2013). Survival times of meter-sized boulders on the surface of the Moon. *Planetary and Space Science*, 89, 118–126. <https://doi.org/10.1016/j.pss.2013.07.011>
- Basilevsky, A. T., Head, J. W., Hörz, F., & Ramsey, K. (2015). Survival times of meter-sized boulders on the surface of airless bodies. *Planetary and Space Science*, 117, 312–328. <https://doi.org/10.1016/j.pss.2015.07.003>
- Boyd, A. K., Robinson, M. S., & Sato, H. (2012). Lunar Reconnaissance Orbiter wide angle camera photometry: An empirical solution. In *Lunar and Planetary Science Conference, 43rd*. Retrieved from <http://www.lpi.usra.edu/meetings/lpsc2012/pdf/2795.pdf>
- Bussey, B., Clarke, S. W., Jenkins, J., & Bailey, B. E. (2019). NASA's lunar discovery and exploration program. *AGUFM, 2019*, PA54B-11.
- Carr, M. H. (1974). The role of lava erosion in the formation of lunar rilles and Martian channels. *Icarus*, 22(1), 1–23. [https://doi.org/10.1016/0019-1035\(74\)90162-6](https://doi.org/10.1016/0019-1035(74)90162-6)
- Chavers, G., Suzuki, N., Smith, M., Watson-Morgan, L., Clarke, S. W., Engelund, W. C., et al. (2019). NASA's human lunar landing strategy. In *70th International Astronautical Congress*.
- Chin, G., Brylow, S., Foote, M., Garvin, J., Kasper, J., Keller, J., et al. (2007). Lunar Reconnaissance Orbiter overview: The instrument suite and mission. *Space Science Reviews*, 129(4), 391–419. <https://doi.org/10.1007/s11214-007-9153-y>
- Donaldson Hanna, K. L., Wyatt, M. B., Thomas, I. R., Bowles, N. E., Greenhagen, B. T., Maturilli, A., et al. (2012). Thermal infrared emissivity measurements under a simulated lunar environment: Application to the Diviner Lunar Radiometer Experiment. *Journal of Geophysical Research*, 117, E00H05. <https://doi.org/10.1029/2011JE003862>
- Elder, C. M., Douglass, B., Ghent, R. R., Hayne, P. O., Williams, J.-P., Bandfield, J. L., & Costello, E. (2019). The subsurface coherent rock content of the Moon as revealed by cold-spot craters. *Journal of Geophysical Research: Planets*, 124, 3373–3384. <https://doi.org/10.1029/2019JE006128>
- Fischer, E. M., & Pieters, C. M. (1996). Composition and exposure age of the Apollo 16 Cayley and Descartes regions from Clementine data: Normalizing the optical effects of space weathering. *Journal of Geophysical Research*, 101, 2225–2234. <https://doi.org/10.1029/95JE02983>
- Ghent, R. R., Hayne, P. O., Bandfield, J. L., Campbell, B. A., Allen, C. C., Carter, L. M., & Paige, D. A. (2014). Constraints on the recent rate of lunar ejecta breakdown and implications for crater ages. *Geology*, 42(12), 1059–1062. <https://doi.org/10.1130/G35926.1>
- Ghent, R. R., Leverington, D. W., Campbell, B. A., Hawke, B. R., & Campbell, D. B. (2005). Earth-based observations of radar-dark crater haloes on the Moon: Implications for regolith properties. *Journal of Geophysical Research*, 110, E02005. <https://doi.org/10.1029/2004JE002366>
- Glotch, T. D., Hagerty, J. J., Lucey, P. G., Hawke, B. R., Giguere, T. A., Arnold, J. A., et al. (2011). The Mairan domes: Silicic volcanic constructs on the Moon. *Geophysical Research Letters*, 38, L21204. <https://doi.org/10.1029/2011gl049548>
- Glotch, T. D., Lucey, P. G., Bandfield, J. L., Greenhagen, B. T., Thomas, I. R., Elphic, R. C., et al. (2010). Highly silicic compositions on the Moon. *Science*, 329, 1510–1513. <https://doi.org/10.1126/science.1192148>
- Greeley, R. (1971). Lunar Hadley Rille: Considerations of its origin. *Science*, 172(3984), 722–725. <https://doi.org/10.1126/science.172.3984.722>
- Greenhagen, B. T., Donaldson Hanna, K., Lucey, P. G., Bowles, N., Isaacson, P., & Milliken, R. (2021). *Diviner Christiansen Feature Map*. Zenodo. <https://doi.org/10.5281/zenodo.4558235>
- Greenhagen, B. T., Lucey, P. G., Bandfield, J. L., Hayne, P. O., Williams, J.-P., & Paige, D. A. (2011). The Diviner Lunar Radiometer compositional data products: Description and examples. In *Lunar and Planetary Science Conference, 42nd*.
- Greenhagen, B. T., Lucey, P. G., Wyatt, M. B., Glotch, T. D., Allen, C. C., Arnold, J. A., et al. (2010). Global silicate mineralogy of the Moon from the Diviner Lunar Radiometer. *Science*, 329, 1507–1509. <https://doi.org/10.1126/science.1192196>
- Grier, J. A., McEwen, A. S., Lucey, P. G., Milazzo, M., & Strom, R. G. (2001). Optical maturity of ejecta from large rayed lunar craters. *Journal of Geophysical Research*, 106(E12), 32847–32862. <https://doi.org/10.1029/1999je001160>
- Hayne, P. O., Bandfield, J. L., Siegler, M. A., Vasavada, A. R., Ghent, R. R., Williams, J.-P., et al. (2017). Global regolith thermophysical properties of the Moon from the Diviner Lunar Radiometer Experiment. *Journal of Geophysical Research*, 122, 2371–2400. <https://doi.org/10.1002/2017JE005387>
- Hayne, P. O., Greenhagen, B. T., Foote, M. C., Siegler, M. A., Vasavada, A. R., & Paige, D. A. (2010). Diviner Lunar Radiometer observations of the LCROSS impact. *Science*, 330(6003), 477–479. <https://doi.org/10.1126/science.1197135>
- Hong, I.-S., Yi, Y., & Kim, E. (2015). Lunar pit craters presumed to be the entrances of lava caves by analogy to the Earth lava tube pits. *Journal of Astronomy and Space Sciences*, 31, 131–140. <https://doi.org/10.5140/JASS.2014.31.2.131>
- Hörz, F., Basilevsky, A. T., Head, J. W., & Cintala, M. J. (2000). Erosion of lunar surface rocks by impact processes: A synthesis. *Planetary and Space Science*, 194, 105105. <https://doi.org/10.1016/j.pss.2020.105105>
- Hörz, F., Grieve, R., Heiken, G., Spudis, P., & Binder, A. (1991). Lunar surface processes. In *Lunar sourcebook: A user's guide to the Moon* (pp. 61–120). Cambridge University Press.
- Kramer, G. Y., Jaiswal, B., Hawke, B. R., Öhman, T., Giguere, T. A., & Johnson, K. (2015). The basalts of Mare Frigoris. *Journal of Geophysical Research: Planets*, 120, 1646–1670. <https://doi.org/10.1002/2014JE004753>
- Lucchitta, B. K., & Watkins, J. A. (1978). Age of graben systems on the Moon. *Proceedings of the Lunar and Planetary Science Conference*, 9, 3459–3472.
- Lucey, P. G., Blewett, D. T., Taylor, G. J., & Hawke, B. R. (2000). Imaging of lunar surface maturity. *Journal of Geophysical Research*, 105(20), 377–20386. <https://doi.org/10.1029/1999JE001110>
- Lucey, P. G., Greenhagen, B., Donaldson Hanna, K., Bowles, N., Flom, A., & Paige, D. A. (2021). Christiansen feature map from the lunar reconnaissance orbiter Diviner Lunar Radiometer experiment: Improved corrections and derived mineralogy. *Journal of Geophysical Research: Planets*, 126, e2020JE006777. <https://doi.org/10.1029/2020JE006777>
- NASA. (2019a). *NASA Selects Experiments for Possible Lunar Flights in 2019*. Retrieved from <https://www.nasa.gov/press-release/nasa-selects-experiments-for-possible-lunar-flights-in-2019>
- NASA. (2019b). *NASA Selects 12 New Lunar Science Technology Investigations*. Retrieved from <https://www.nasa.gov/press-release/nasa-selects-12-new-lunar-science-technology-investigations>
- Ostrach, L. (2011). *Rimae Bürg*. Retrieved from <http://roc.sese.asu.edu/posts/289>
- Paige, D. A. (2010). LRO DLRE LEVEL 4 RDR V1.0, NASA Planetary Data System, LRO-L-DLRE-4-RDR-V1.0. <https://doi.org/10.17189/1520651>
- Paige, D. A., Foote, M. C., Greenhagen, B. T., Schofield, J. T., Calcutt, S., Vasavada, A. R., et al. (2010). The Lunar Reconnaissance Orbiter Diviner Lunar Radiometer Experiment. *Space Science Reviews*, 150(1–4), 125–160. <https://doi.org/10.1007/s11214-009-9529-2>
- Paige, D. A., Siegler, M. A., Zhang, J. A., Hayne, P. O., Foote, E. J., Bennett, K. A., et al. (2010). Diviner Lunar Radiometer Observations of cold traps in the Moon's south polar region. *Science*, 330(6003), 479–482. <https://doi.org/10.1126/science.1187726>
- Pizer, S. M., Amburn, E. P., Austin, J. D., Cromartie, R., Geselowitz, A., Greer, T., et al. (1987). Adaptive histogram equalization and its variations. *Computer Vision, Graphics, and Image Processing*, 39, 355–368. [https://doi.org/10.1016/S0734-189X\(87\)80186-X](https://doi.org/10.1016/S0734-189X(87)80186-X)

- Robinson, M. S., Brylow, S. M., Tschimmel, M., Humm, D., Lawrence, S. J., Thomas, P. C., et al. (2010). Lunar Reconnaissance Orbiter Camera (LROC) instrument overview. *Space Science Reviews*, 150, 81–124. <https://doi.org/10.1007/s11214-010-9634-2>
- Roush, T. L., Colaprete, A., Cook, A., Bielawski, R., Ennico-Smith, K., Benton, J., et al. (2020). NIRVSS aboard CLPS. In *51st Lunar and Planetary Science Conference*.
- Roush, T. L., Colaprete, A., Elphic, R., Ennico-Smith, K., Heldmann, J., Stoker, C., et al. (2015). In Situ Resource Utilization (ISRU) field expedition 2012: Near-Infrared Volatile Spectrometer System (NIRVSS) science measurements compared to site knowledge. *Advances in Space Research*, 55(10), 2451–2456. <https://doi.org/10.1016/j.asr.2014.08.033>
- Russell, P. S., Paige, D. A., & Greenhagen, B. T. (2017). Thermophysical behavior of the uppermost lunar surface from Diviner high time-resolution, post-sunset observations. In *48th Lunar and Planetary Science Conference*.
- Russell, P. S., Paige, D. A., & Greenhagen, B. T. (2019). Thermophysical behavior of the uppermost lunar surface from Diviner high time-resolution, post-sunset observations. In *50th Lunar and Planetary Science Conference*.
- Scott, D. H. (1972). Geologic map of the Eudoxus Quadrangle of the Moon. In *U.S. Geological Survey Miscellaneous Investigations Series Map I-705*.
- Sefton-Nash, E., Williams, J.-P., Greenhagen, B. T., Aye, K.-M., & Paige, D. A. (2017). Diviner Lunar Radiometer gridded brightness temperatures from geodesic binning of modeled fields of view. *Icarus*, 298, 98–110. <https://doi.org/10.1016/j.icarus.2017.04.007>
- Smith, D. E., Zuber, M. T., Neumann, G. A., Lemoine, F. G., Mazarico, E., Torrence, M. H., et al. (2010). Initial observations from the Lunar Orbiter Laser Altimeter (LOLA): LOLA initial observations. *Geophysical Research Letters*, 37, L18204. <https://doi.org/10.1029/2010GL043751>
- Speyerer, E. J., Robinson, M. S., & Denevi, B. W., & LROC Team. (2011). Lunar Reconnaissance Orbiter Camera Morphological Map of the Moon. In *Lunar and Planetary Science Conference*, 42nd. Retrieved from <https://www.lpi.usra.edu/meetings/lpsc2011/pdf/2387.pdf>
- Sullivan, M. T., Paige, D. A., Arvidson, R. E., & Grayzeck, E. (2020). *Lunar Reconnaissance Orbiter Diviner Lunar Radiometer Experiment: Reduced data record and derived Products Software Interface Specification* (Technical Report Version 1.15). PDS Geosciences Node.
- Terada, K., Morota, T., & Kato, M., (2020). Asteroid shower on the Earth-Moon system immediately before the Cryogenian period revealed by KAGUYA. *Nature Communications*, 11, 3453. <https://doi.org/10.1038/s41467-020-17115-6>
- Thornton, J., Huber, S., Peterson, K., & Hendrickson, D. (2015). Astrobotic: Commercial service for lunar resource payload delivery. In *Annual Meeting of the Lunar Exploration Analysis Group* (Vol. 1863, p. 2066).
- Tooley, C. R., Houghton, M. B., Saylor, R. S., Peddie, C., Everett, D. F., Baker, C. L., & Safdie, K. N. (2010). Lunar Reconnaissance Orbiter mission and spacecraft design. *Space Science Reviews*, 150(1–4), 23–62. https://doi.org/10.1007/978-1-4419-6391-8_4
- Vasavada, A. R., Bandfield, J. L., Greenhagen, B. T., Hayne, P. O., Siegler, M. A., Williams, J.-P., & Paige, D. A. (2012). Lunar equatorial surface temperatures and regolith properties from the Diviner Lunar Radiometer Experiment. *Journal of Geophysical Research*, 117, E00H18. <https://doi.org/10.1029/2011JE003987>
- Vondrak, R., Keller, J., Chin, G., & Garvin, J. (2010). Lunar Reconnaissance Orbiter (LRO): Observations for lunar exploration and science. *Space Science Reviews*, 150(1–4), 7–22. https://doi.org/10.1007/978-1-4419-6391-8_3
- Voosen, P. (2018). NASA to pay private space companies for moon rides. *Science*, 362(6417), 875–876. <https://doi.org/10.1126/science.362.6417.875>
- Wagner, R. V., & Robinson, M. S. (2012). Computer-assisted detection of collapse pits in LROC NAC Images. *AGU Fall Meeting*, P53A-2042. Retrieved from <https://ui.adsabs.harvard.edu/abs/2012AGUFM.P53A2042W>
- Wagner, R. V., & Robinson, M. S. (2014). Distribution, formation mechanisms, and significance of lunar pits. *Icarus*, 237, 52–60. <https://doi.org/10.1016/j.icarus.2014.04.002>
- Wagner, R. V., Speyerer, E. J., & Robinson, M. S., & LROC Team. (2015). New mosaicked data products from the LROC team. In *Lunar and Planetary Science Conference*, 46th. Retrieved from <https://www.hou.usra.edu/meetings/lpsc2015/pdf/1473.pdf>
- Warren, T. J., Bowles, N. E., Donaldson Hanna, K., & Bandfield, J. L. (2019). Modeling the angular dependence of emissivity of randomly rough surfaces. *Journal of Geophysical Research: Planets*, 124, 585–601. <https://doi.org/10.1029/2018JE005840>
- Wilhelms, D. E. (1987). The geologic history of the Moon. In *U.S. Geological Survey Professional Paper 1348* (p. 302). <https://doi.org/10.3133/pp1348>
- Williams, J.-P., Bandfield, J. L., Paige, D. A., Powell, T. M., Greenhagen, B. T., Taylor, S., et al. (2018). Lunar cold spots and crater production on the moon. *Journal of Geophysical Research: Planets*, 123, 2380–2392. <https://doi.org/10.1029/2018JE005652>
- Williams, J. P., Greenhagen, B. T., Paige, D. A., Schorghofer, N., Sefton-Nash, E., Hayne, P. O., et al. (2019). Seasonal polar temperatures on the Moon. *Journal of Geophysical Research: Planets*, 124, 2505–2521. <https://doi.org/10.1029/2019JE006028>
- Williams, J.-P., Paige, D. A., Greenhagen, B. T., & Sefton-Nash, E. (2017). The global surface temperatures of the Moon as measured by the Diviner Lunar Radiometer Experiment. *Icarus*, 283, 300–325. <https://doi.org/10.1016/j.icarus.2016.08.012>
- Williams, J.-P., Sefton-Nash, E., & Paige, D. A. (2016). The temperatures of Giordano Bruno crater observed by the Diviner Lunar Radiometer Experiment: Application of an effective field of view model for a point-based data set. *Icarus*, 273, 205–213. <https://doi.org/10.1016/j.icarus.2015.10.034>